PERGAMON

Deep-Sea Research II 50 (2003) 2285–2304

DEEP-SEA RESEARCH
PART II

www.elsevier.com/locate/dsr2

Variability of the depth of the 20°C isotherm along 6°N in the Bay of Bengal: its response to remote and local forcing and its relation to satellite SSH variability

Lisan Yu

Department of Physical Oceanography, MS# 21, Woods Hole Oceanographic Institution, Woods Hole, MA 02543, USA

Abstract

The depth of the 20°C isotherm (hereafter referred to as D20) derived from expendable bathythermograph (XBT) measurements along 6°N in the southern Bay of Bengal (hereafter referred to as the Bay) shows pronounced seasonal-to-interannual variability and profound westward propagation. But not all these features are well depicted by satellite observations of sea-surface height (SSH). The cause of the thermocline variability for the period of 1988–1999 and the relationship to SSH variability were analyzed in this study with the addition of wind and salinity data sets.

Local Ekman pumping and remote Kelvin/Rossby wave propagation are the two leading forcing mechanisms for the thermocline variability at the chosen XBT section. On seasonal timescales, the phase of the D20 semiannual variations is determined by a remote forcing signal, but the amplitude is determined by interaction with the annual background that is preconditioned by the local Ekman pumping. The local background has the phase oscillating in a way that it enhances the westward propagation of the remote semiannual signal during the first half of the year but suppresses the semiannual signal during the second half of the year. On interannual timescales, the D20 at 6°N is most sensitive to the remote equatorial wind variability, with local forcing variability being a secondary contributor. This study shows that the calculation of the Ekman pumping velocity should include the contribution from not only wind-stress curl but also zonal wind stress due to the β-effect at 6°N. Omitting the latter would augment the effect of local forcing.

The relationship between satellite SSH and D20 is not linear in the Bay, as large salinity variation contributes considerably to the SSH variability. Compared to the structure of seasonal D20 anomalies, the SSH anomalies are more zonally aligned, less westward propagating, and have a weak semiannual signal. A relationship between the sea level and thermocline variation is derived by using a two-layered system that includes seasonal variations of temperature and salinity in upper-ocean density. This allows the structure of the satellite SSH to be examined from the XBT temperature and the salinity climatology and enables salinity effect to be quantified. At 6°N the amplitude of the SSH variations induced by the salinity effect is about 3 cm, equivalent to the amplitude induced by the temperature effect.

1. Introduction

The Bay of Bengal is a semi-enclosed basin that comes under the strong influence of the annual reversing monsoon. The Bay is also influenced by remote equatorial Kelvin waves due to its direct contact with the equator along the eastern boundary. Numerical model analyses have shown that the remotely forced waves play a dominant role in driving the reversal of the upper-ocean

E-mail address: lyu@whoi.edu (L. Yu).

0967-0645/03/$ - see front matter
doi:10.1016/S0967-0645(03)00057-2

circulation from anticyclonic structure during the northeast monsoon to cyclonic structure during the southwest monsoon (Yu et al., 1991; Potemra et al., 1991; Hacker et al., 1998), yet numerical studies have also credited the role of local wind forcing (McCreary et al., 1993, 1996; Shankar et al., 1996). In situ measurements have been used to validate the hypotheses, but they were mostly confined to slope and shelf regions along the periphery of the Bay (e.g., Shetye et al., 1993; Clarke and Liu, 1993). Satellite observations of sea-surface height (SSH) have been introduced recently (Yang et al., 1998; Basu et al., 2000; Eigenheer and Quadfasel, 2000), but the lack of resolution near the coast may cripple the detection of coastal Kelvin wave signals (Fu and Cheney, 1995), and the large salinity variation may bias the SSH representation of the thermocline variability (Maes, 1998; Ji et al., 2000). How remote and local forcing are combined on seasonal timescales is important, as this is the first step toward understanding the Bay's interannual variability. How much SSH variability can be interpreted as thermocline variability is also important, as the SSH with its continuous, basin-wide coverage promises an integral view of the upper-ocean circulation in the poorly observed Bay interior. These two questions are examined in this study using temperature profiles acquired from expendable bathythermographs (XBT) along commercial ship tracks in the southern Bay and equatorial region.

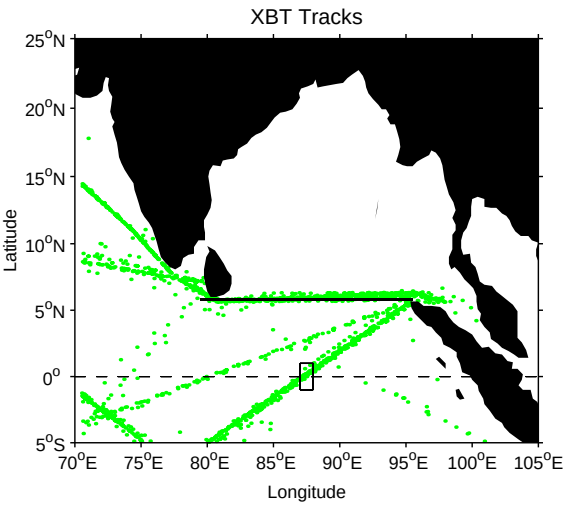

Fig. 1. Map of the Bay of Bengal with locations of ship tracks. The XBT profiles collected along 6°N (marked by a straight line) and at the equatorial position (marked by a rectangle) are used.

2. Data description

2.1. Processing of XBT profiles

A total of 3785 XBT profiles were received along 6°N between Sri Lanka (80°E) and Malacca Strait (95°E) (Fig. 1) for the period between November 1987 and December 1999. The ship route, being part of the XBT network established in 1985 under the auspices of the international TOGA/WOCE program, is the only place over the entire Bay where long-term upper-ocean samplings can be found. Ship records were available for each month except in June 1993 and July 1995. Almost all the profiles extend deeper than 400 m, but the samples are irregular in time and space and contaminated by high-frequency variability. To construct a monthly temperature section for the upper 400 m, it was necessary to conduct quality control, gridding, interpolating, and smoothing, but processing was kept minimal to avoid smoothing out true signals. All profiles were first plotted and those with obvious errors were removed. The profiles were then linearly interpolated onto every 5 m level in the vertical and binned onto a 1° grid along 6°N. Linear interpolation was applied to fill void points. A three-point filter with weights $[\frac{1}{4}, \frac{1}{2}, \frac{1}{4}]$ was applied in space and then in time to further smooth the gridded data at each level.

The zonal alignment of the section suits the need of examining the westward propagating Rossby waves and their interaction with local forced response. Vinayachandran et al. (1999a) have used the climatological state of this section to study the seasonal southwest monsoon current and associated mass transport that enter the Bay from the Arabian Sea during summer (Schott et al., 1994). This section can also be linked to the XBT profiles acquired near the equator to examine the propagation of remotely forced wave signals. However,

XBT profiles in the equatorial region were available only when commercial ships crossed the equator (Fig. 1). Given the limited number of such ship tracks, the samples were not sufficient to compose a section along the equator. Instead, the strategy was to pick a location where measurements were dense enough to make a reliable time series at least on seasonal timescales. For this reason, the profiles collected in the area within [86–87°E, 1°S–1°N] (marked by a rectangle in Fig. 1) by ships traveling between Malacca Strait and Madagascar were processed. Observations along this ship route have been used by Yu and Rienecker (2000) to study the response of the thermocline during the Indian Ocean warming event in 1997–1998. A total of 546 profiles was received for the 1988–1999 period. But with many months missing in the data set, only the time series for the 12-year monthly mean could be constructed.

2.2. Sources of other data sets

- SSH: The altimetry data produced by the NASA Ocean Altimeter Pathfinder Project (Koblinsky et al., 1998, 1999) were used to assess their relationship with the thermocline variability observed from XBTs. The data contain $1^\circ \times 1^\circ$ gridded monthly SSH anomalies derived from the 1993–1996 mean state. Corrections and calibrations were conducted using community consensus algorithms.
- Sea-surface winds: The winds were produced by Atlas et al. (1996) through objectively blending wind speed observations derived from the Defense Mapping Satellite Program Special Sensor Microwave Imager (SSMI), wind vectors observed from ships and buoys, and surface wind analyses produced from the European Center for Medium Range Weather Forecasts (ECMWF). The data are available at 6-hourly interval with a spatial resolution of 1° in both longitude and latitude. Monthly data were constructed and used to compute wind stress and stress curl fields with a drag coefficient of 1.2×10^{-3}. Monthly anomalies of these fields were calculated using the 1988–1999 base period monthly means.
- World ocean atlas (WOA) (Levitus and Boyer, 1994): The monthly climatology is the only known source of salinity data for the Bay. The information was integrated with XBT temperature measurements to quantify the effect of salinity on the seasonal variability of SSH.

2.3. Mean characteristics of the vertical density structure at 6°N

By using the equation of state of seawater (Millero and Poisson, 1981; UNESCO, 1981), the mean density structure in the upper 400 m at 6°N was calculated (Fig. 2c) from the XBT temperature averaged over the 12-year period 1988–1999 (Fig. 2a) and the WOA salinity climatology (Fig. 2b). A sharp pycnocline exists that separates the shallow warm and fresh layer from the cool and salty water in the deeper ocean. It can be seen that the depth of the 20°C isotherm (D20) is a proper index for the thermocline variability and also a good proxy for the pycnocline variability. The two-layer character of the density structure provides a base for laying out a reduced gravity model configuration for the analysis in this study. Such a model (Fig. 2d) can be described as a dynamically active layer with density ρ_1 and a deep motionless layer with a higher density ρ_2. The mean depth of the D20 is denoted by H, the variation of the sea level by η, and the vertical displacement between the two layers by h_d.

3. Seasonal variability

3.1. Seasonal variability of local and remote wind forcing

The seasonal evolution of zonal and meridional components of the wind stress, (τ^x, τ^y), and wind-stress curl, curl(τ), along 6°N in the Bay was plotted (Figs. 3a–c). The local forcing has an annual cycle associated with the annual reversal of the monsoon over the Bay (Figs. 4a–b). The winds change from southwesterlies during April–October to northeasterlies during November–March, and the wind-stress curl reverses correspondingly. It is interesting to note that the curl pattern is 180° out

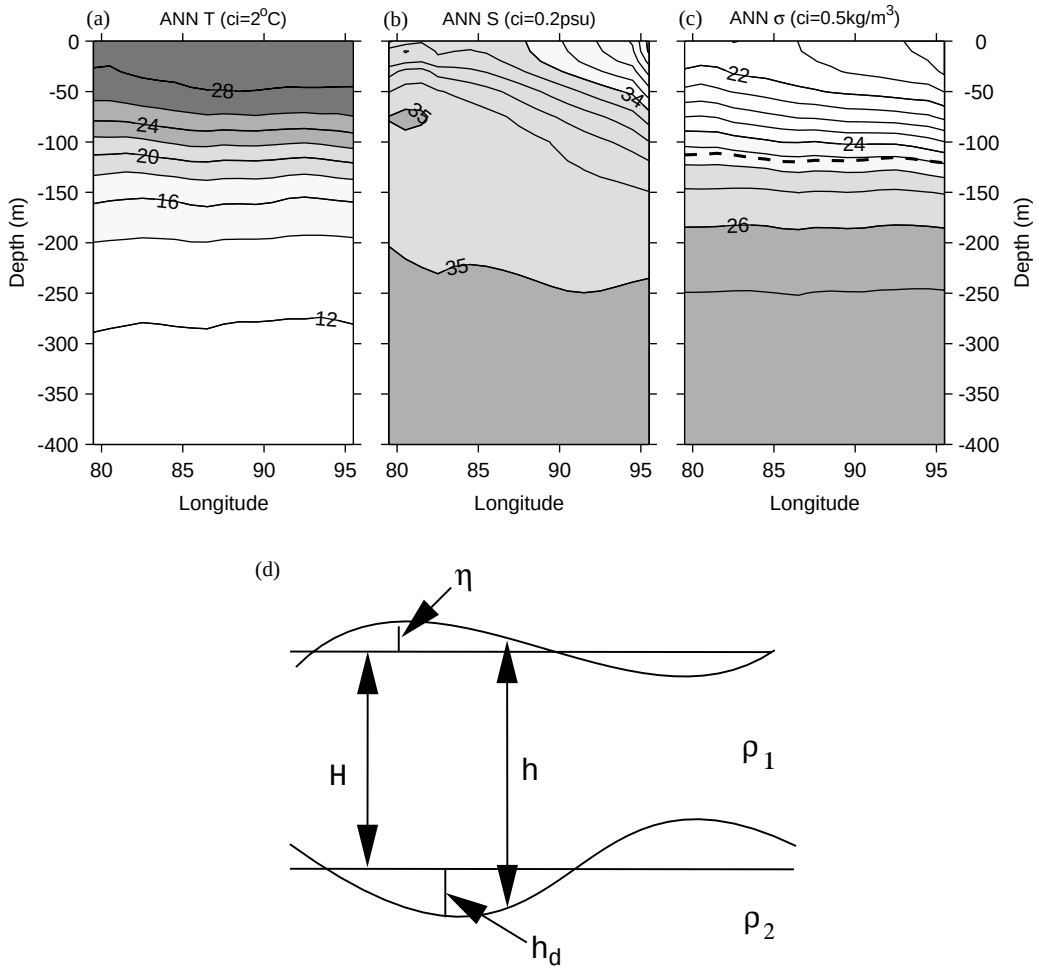

Fig. 2. Annual means of (a) the XBT temperature (ci = 2°C), (b) WOA salinity (ci = 0.2 psu), and (c) the density calculated using (a) and (b) (ci = 0.5 kg/m^3) in the upper 400 m. The location of the D20 is superposed in (c) as a dashed line. A two-layered system that can be used to approximate the D20 variability is schematically depicted in (d).

of phase on the two sides of 83°E, due to the apparent influence of the Sri Lankan land mass. The curl is anticyclonic (negative) east of Sri Lanka but cyclonic (positive) around Sri Lanka during April–October, and the pattern reverses sign during November–March.

Along the equator, the zonal wind stress in the central and eastern region has a semiannual periodicity (Fig. 3d). The winds switch direction four times a year, being easterlies during the two monsoons (northeast monsoon during December–March and southwest monsoon during June–September) and westerlies during the two monsoonal transitions (April–May and October–November). These winds excite propagating Kelvin and Rossby waves that travel great distances to affect the ocean in remote regions (Lighthill, 1969; Cane and Sarachik, 1981; Schott and McCreary, 2001). Yu et al. (1991) and Potemra et al. (1991) have shown that this "teleconnection mechanism" applies to the Indian Ocean, where the equatorial Kelvin waves contribute to the seasonal gyre circulation in the Bay through reflected Rossby waves.

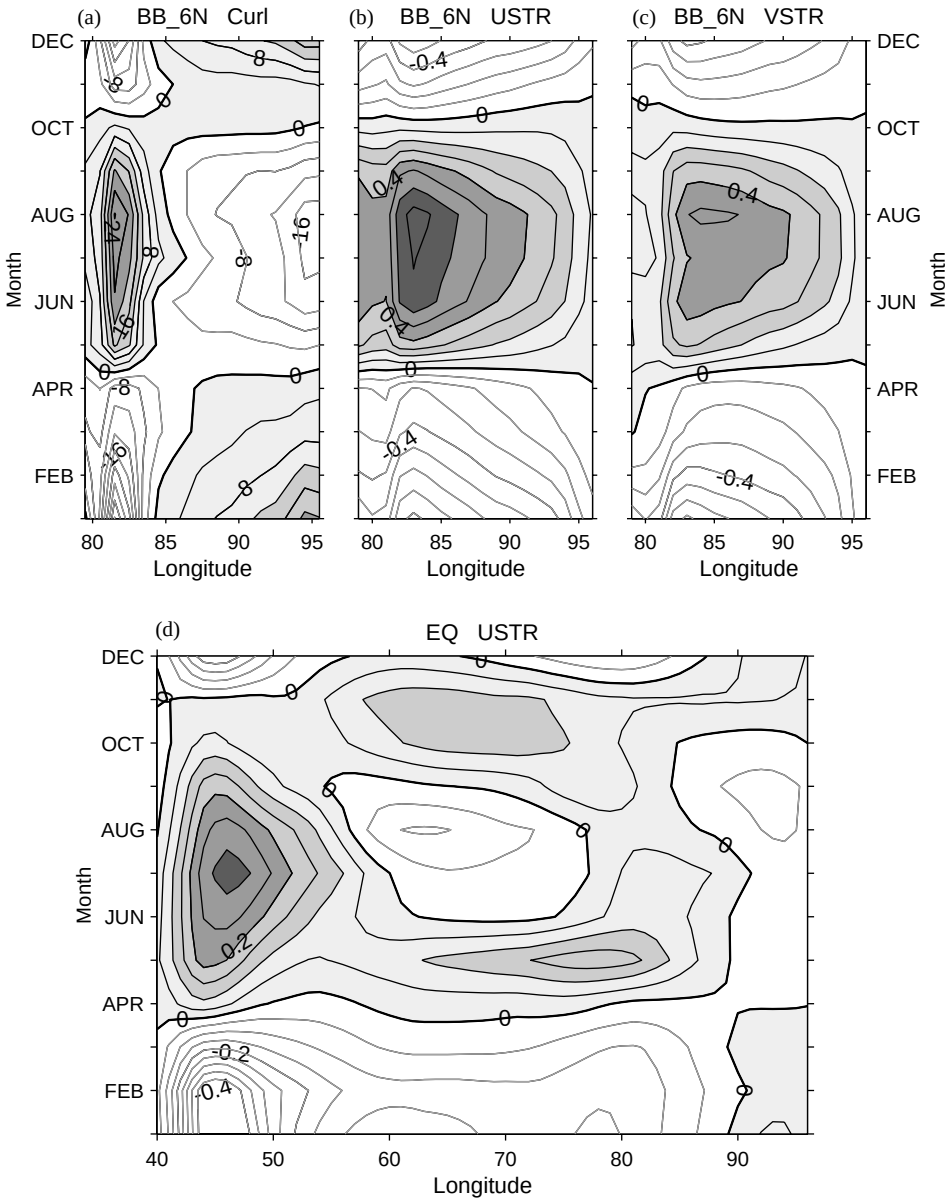

Fig. 3. Seasonal variations (annual mean removed) of (a) wind-stress curl (ci = 4×10^{-9} dyn/cm^3), (b) zonal wind-stress component (ci = 0.1 dyn/cm^2), (c) meridional wind-stress component (ci = 0.1 dyn/m^2) along 6°N in the Bay, and (d) zonal wind-stress component along the equator (ci = 0.05 dyn/cm^2).

3.2. Characteristics of the D20 variability at 6°N

Large seasonal anomalies are observed in the subsurface temperatures (Fig. 5) near 100 m where the main thermocline is located (Fig. 2a). The anomalies originate from the eastern boundary and have a westward propagation. The propagation of negative anomalies starts in January and the amplitude strengthens in the interior, while positive anomalies come into the region in May

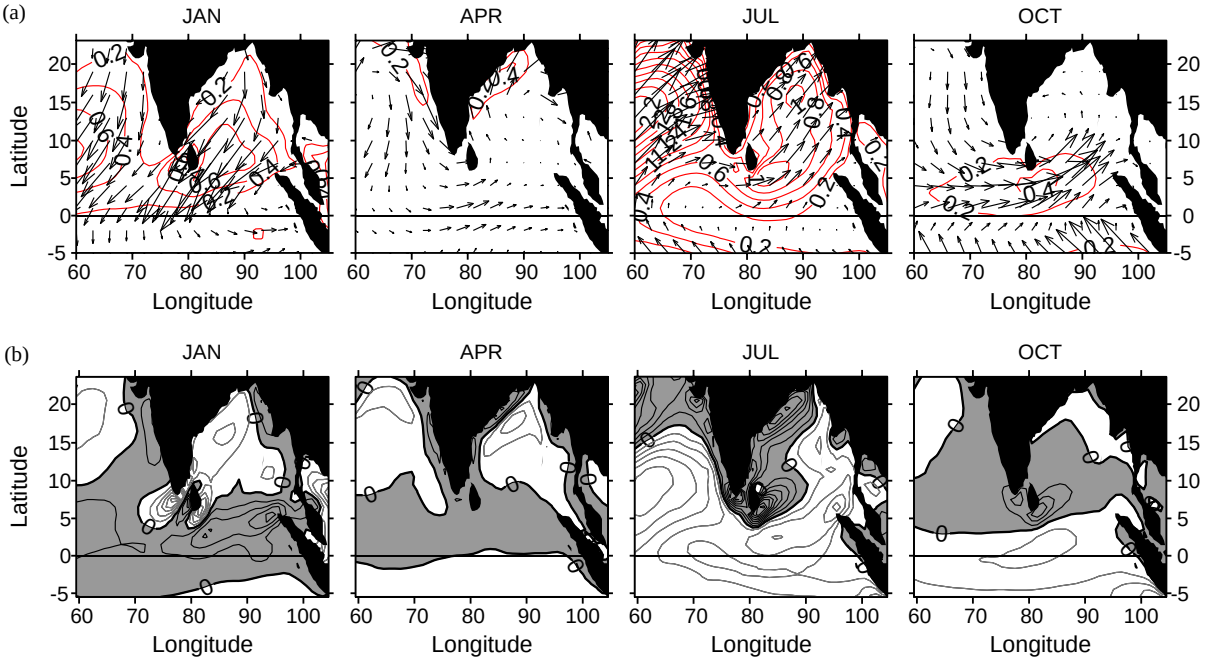

Fig. 4. Spatial structures (annual mean removed) of (a) monthly wind-stress vector and amplitude (ci = 0.2 dyn/cm^2) and (b) monthly wind-stress curl (ci = 5×10^{-9} dyn/cm^3) in January, April, July, and October in the Bay of Bengal. Positive anomalies in (b) are shaded.

and also undergo strengthening after leaving the eastern boundary. The subsurface temperatures in the central section change from ~2°C below the annual mean during February–May to ~2°C above the mean during May–August. Between August and January, a second cycle exists with negative anomalies leaving the eastern boundary in August and positive anomalies in October, but the amplitude is not as large as that in the first cycle.

The emanation of the semiannual signal from the eastern boundary and the westward propagation of the signal are clearly depicted in the time–longitude plot of the seasonal variations of the D20 (Fig. 6a). It shows that there is about 16 m change in the D20 corresponding to the 2°C change in the subsurface temperature. It is evident that the first semiannual cycle is strong with the maximum amplitude located in the interior, and that the second cycle is weaker with the maximum amplitude near the eastern boundary. However, the semiannual signals are confined only to the east of Sri Lanka. Near Sri Lanka, the D20 possesses an annual cycle with one maximum and one minimum per year.

3.3. Contributions of local and remote forcing processes

The physical processes that govern the interior thermocline variability include the wind-stress curl through the mechanism of Ekman pumping, the radiation of westward propagating Rossby waves as a result of such pumping, and the radiation of Rossby waves from poleward propagating coastal Kelvin waves along the eastern boundary (Meyers, 1975, 1979; White, 1977; Kessler, 1990). In the Bay, coastal Kelvin waves are composed of both locally forced signals that are induced by alongshore monsoon wind stress and remotely forced Kelvin wave signals that propagate from the equator. The combination of local and remote signals (Fig. 3) gives rise to different D20 responses on the two sides of 83°E: an annual periodicity near Sri Lanka and a semiannual periodicity in the central and eastern part of the

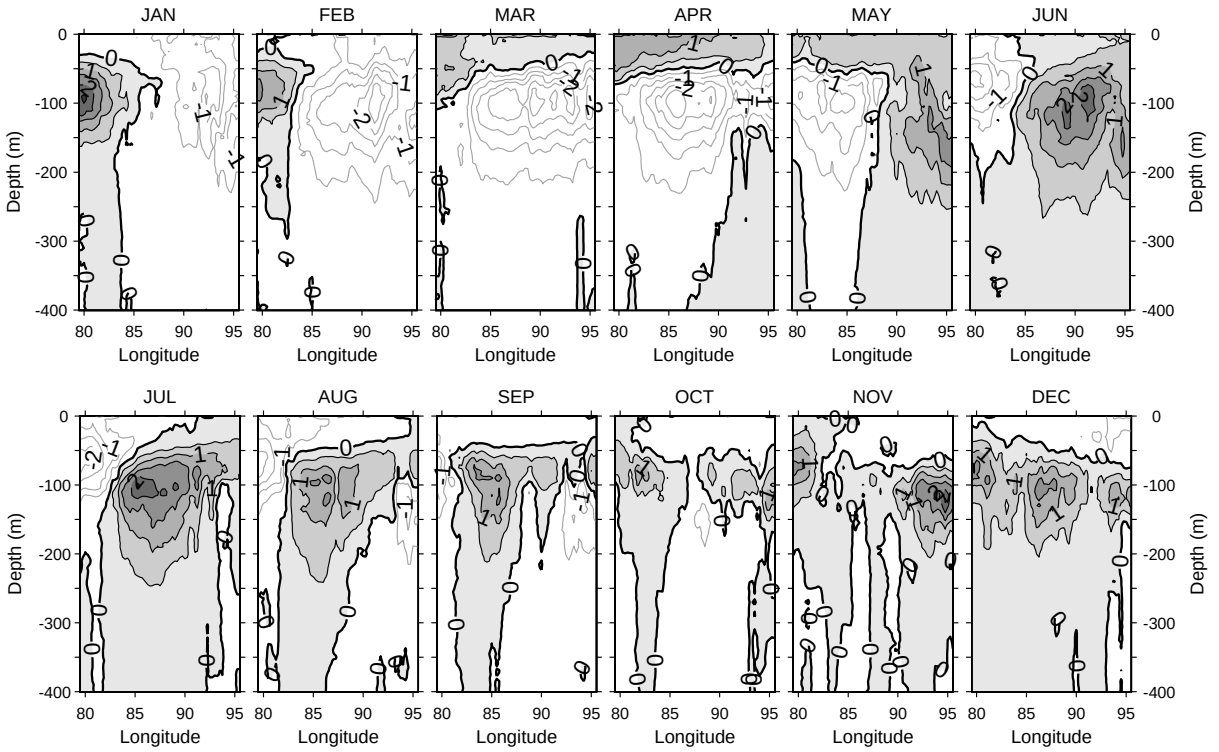

Fig. 5. Seasonal variations (annual mean removed) of the vertical temperature structure constructed from 12-year XBT profiles (ci = 0.5°C). Positive anomalies are shaded and negative anomalies are contoured with gray lines.

section (Fig. 6a). How can the D20 have a selective response to multi-frequency forcing signals? In other words, what are the roles of remote and local forcing in the two regions? To answer these questions, a vorticity equation that describes essential time-dependent β-plane dynamics for a $1\frac{1}{2}$-layer-reduced gravity model (Fig. 2d) (White, 1977; Meyers, 1979; Kessler, 1990) is used. The equation can be written as

$$h_t + c_R h_x = W_E, \quad \text{where} \quad W_E = -\frac{1}{\rho_1}\text{curl}\left(\frac{\tau}{f}\right), \tag{1}$$

where h denotes the thermocline variability, c_R the zonal phase speed of the nondispersive Rossby waves, and W_E the Ekman pumping velocity. By best-fitting a line to XBT observations, c_R is estimated at 24 cm s^{-1}. This is close to the phase speed of the second mode baroclinic Rossby waves, whose theoretical estimate is about 21 cm s^{-1} (Yang et al., 1998). The dominance of the second mode baroclinic waves in the Indian Ocean variability has been shown by McCreary et al. (1993). The Ekman pumping velocity, W_E, can be further expressed as

$$\frac{1}{\rho_1}\text{curl}\left(\frac{\tau}{f}\right) \equiv \frac{\text{curl}(\tau)}{\rho_1 f} + \frac{\beta\tau^x}{\rho_1 f^2}, \tag{2}$$

where β is the meridional gradient of the Coriolis parameter f. Eq. (2) states that the Ekman pumping velocity on the β-plane includes the contributions from both wind-stress curl and direct wind-stress forcing. The ratio between the two contributions is (Pedlosky, 1996):

$$O\left(\frac{\text{curl}(\tau)/\rho_1 f}{\beta\tau^x/\rho_1 f^2}\right) = O\left(\frac{f}{\beta L}\right) = O\left(\frac{R}{L}\tan\theta\right), \tag{3}$$

where L, the length scale of the wind stress associated with the monsoon circulation in the Indian Ocean, is not more than 1000 km and much smaller than the earth's radius R ($\sim$6400 km).

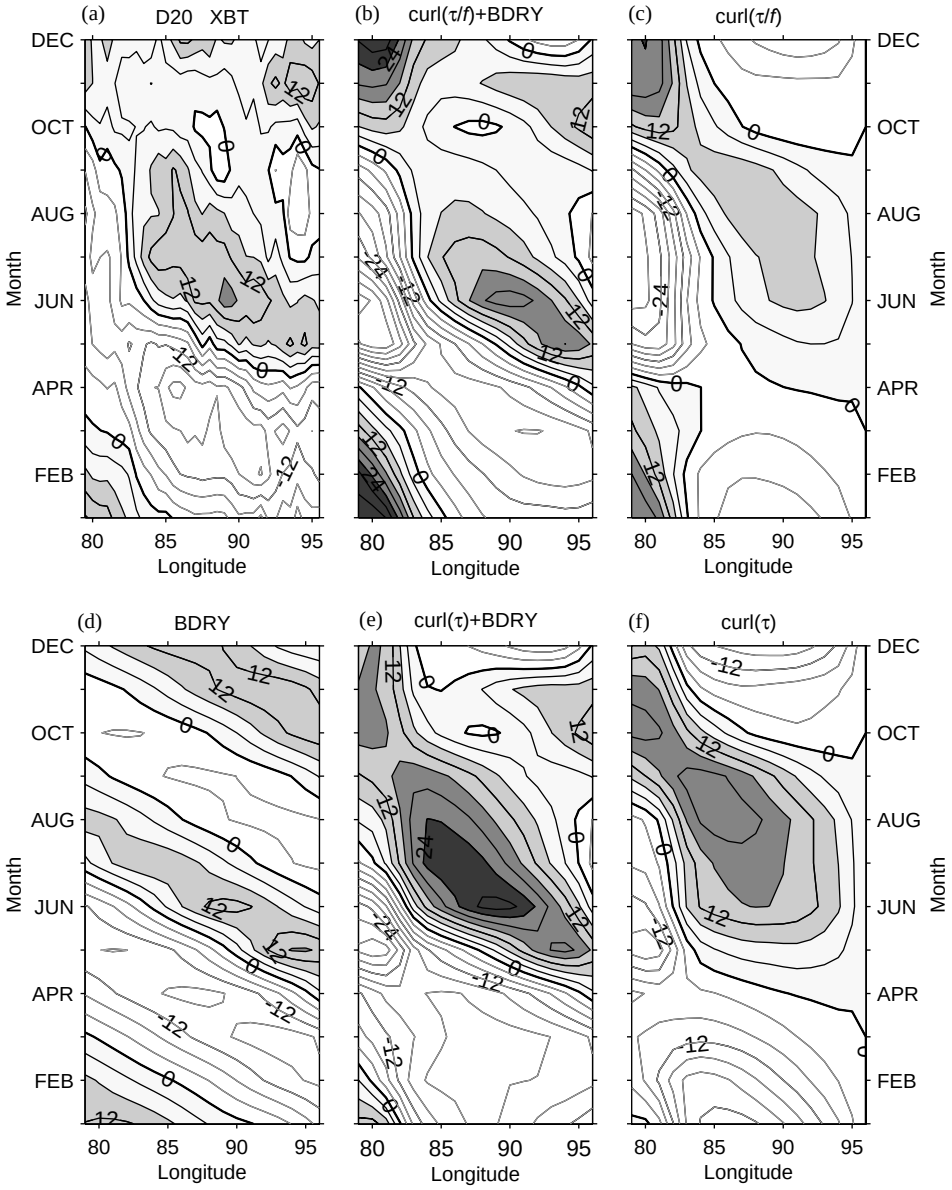

Fig. 6. Seasonal variations (annual mean removed) of D20 from (a) observations and a series of model analyses that include the calculation (b) using curl(τ/f) forcing and the observed boundary condition, (c) using curl(τ/f) forcing with zero boundary condition, (d) using the specified boundary condition with no wind forcing, (e) using curl(τ) forcing and the observed boundary condition, and (f) using curl(τ) forcing with zero boundary condition. The contour interval is 4 m for all plots. Positive anomalies are shaded and negative anomalies are contoured with gray lines.

However, at the XBT section at $\theta = 6°$N, the small θ forces the ratio to be 0.67 and demands the inclusion of the contribution from the direct wind-stress forcing induced by the β-effect. In the following, we use curl(τ/f) to indicate that the term is included in the calculation of W_E; otherwise, we use the term curl(τ).

Eq. (1) allows for the investigation of the thermocline variations due to local Ekman pumping effect and nondispersive Rossby wave

propagation while subject to the specification of the eastern boundary condition. This permits the remote forced signals, which are not included in the model physics, to be considered in the boundary processes and then carried westward by Rossby waves to interact with locally forced signals away from the boundary. Eq. (1) has linear dynamics and so responses to remote and local forcing can be diagnosed separately. A total of five experiments were designed to test the response of the D20 to the boundary forcing, to W_E calculated from curl(τ/f) forcing, to the combination of W_E and boundary forcing, and to the W_E calculated from curl(τ/f) forcing with and without the boundary forcing. Following the studies of Masumoto and Meyers (1998), the observed D20 anomaly at 95°E was taken as the eastern boundary condition.

The results from the five experiments are plotted in Figs. 6b–f. They show that the D20 calculated from Eqs. (1) and (2) with the imposed observational signal at the eastern boundary (Fig. 6b) reproduces remarkably well the phase and amplitude of the observed D20 semiannual cycle in the central and eastern section (Fig. 6a). The pattern of the D20 in Fig. 6b is the superposition of the D20 response to annual W_E with the eastern boundary set at zero (Fig. 6c) and the response to the westward propagation of the eastern boundary semiannual signal with W_E set at zero (Fig. 6c). During April–September, the downwelling phase (positive D20 anomalies) produced by W_E enhances the downwelling signal that leaves the boundary between April and June but suppresses the upwelling signal that leaves the boundary between July and August. The upwelling phase (negative D20 anomalies) generated by the Ekman pumping during October–March has the same amplifying (reducing) effect on the semiannual signal of the same (opposite) sign. Clearly, the phase of the semiannual signal is propagated from the eastern boundary, but the amplitude is determined by its interaction with the annual background that is preconditioned by local Ekman pumping W_E. As the effect of the Ekman pumping on the D20 is largest in the interior and the effect of the boundary signal is largest close to the eastern boundary, the superposition of the two signals yields a maximum amplitude in the interior if they have the same sign but confines the amplitude near the eastern boundary if they have opposite sign.

The differences between the two sets of experiments that use curl(τ) instead of curl(τ/f) in calculating W_E are clearly presented (Fig. 6e): near Sri Lanka the phase of the annual cycle is shifted ahead by 1–2 months, and in the interior the amplitude of the semiannual cycle between January and September is significantly enhanced. This is because the response of the D20 to W_E associated with curl(τ) forcing is almost twice as large as that to W_E associated with curl(τ/f), especially to the west of 90°E (Fig. 6f). The large amplitude dominates the signal propagating from the boundary (Fig. 6d) and conceals the role of the remote forcing in the interior. It appears that the contribution to W_E from direct wind-stress forcing induced by the β-effect is opposite to the contribution from the curl(τ) forcing. If neglected, the role of local forcing would be exaggerated.

The simulated D20 near Sri Lanka has larger amplitude than the observations when W_E is included (Figs. 6b–f), although the annual cycle is well simulated especially by W_E using curl(τ/f) forcing. This problem exists because the simple model in Eq. (1) does not have coastal Kelvin waves at the western boundary that otherwise would carry the mass away southward. Nevertheless, the experiments indicate that the local Ekman pumping dictates the annual phase of the D20 near Sri Lanka, while the semiannual signal from the eastern boundary, being weakened during westward propagation, causes only a slight modification to the annual amplitude. This is consistent with the finding that Ekman pumping is the major contributor to the formation of the cold Sri Lanka dome during the southwest monsoon (McCreary et al., 1996; Vinayachandran and Yamagata, 1998).

This analysis shows that the simple model (1) is quite successful in simulating the observed D20 variability and in obtaining a pattern of interaction. It is found that the local annual cycle enhances the remote semiannual signal that arrives at the eastern boundary during the first half of the year but weakens the semiannual

signal that arrives during the second half of the year.

3.4. The relation of local D20 variability to remote equatorial wind forcing variability

An attempt was made here to connect the semiannual variability of the D20 at 6°N to that on the equator to examine the signal propagation away from the origin. To do so, we constructed the time series of the D20 and zonal wind stress averaged over the equatorial box [86–87°E, 1°S–1°N] (hereafter referred to as $D20_{[EQ]}$ and $USTR_{[EQ]}$) and the time series of D20 obtained at the two Bay locations, [92°E, 6°N] and [86°E, 6°N] (hereafter referred to as $D20_{[92,6]}$ and $D20_{[86,6]}$, respectively). The equatorial location was chosen simply because of the existence of sufficient number of XBT profiles for constructing monthly variability (see Section 2). But in choosing the Bay locations two considerations were given. First, if the phase speed of the second baroclinic Kelvin waves is estimated at 1.4 m/s (Yang et al., 1998) and that of the Rossby waves at 6°N is given at 0.24 m/s (Fig. 6a), approximately 1 month is needed for the signal to propagate from the equatorial location to the Bay location at [92°E, 6°N] and 2 months to the location at [86°E, 6°N]. The phase shifts on those monthly timescales can be better resolved by using the monthly XBT data. Second, the maximum local forcing effect is in the interior while the maximum remote effect is near the eastern boundary. The two chosen locations, one near the eastern boundary and the other in the interior, allow the examination of signal propagation.

The correlation of the time series of the D20 at the three chosen locations is shown in Fig. 7a. A 1-month lag between $D20_{[92,6]}$ and $D20_{[EQ]}$ and a 2-month lag between $D20_{[86,6]}$ and $D20_{[EQ]}$ are clearly displayed, which support the present analysis that the semiannual signal from the equatorial region determines the phase of the semiannual periodicity along 6°N in the Bay. This assessment of the role of local forcing in modulating the amplitude of the semiannual signal is also corroborated: the $D20_{[92,6]}$ and $D20_{[86,6]}$ show a westward enhancement during January–September and their amplitudes are larger than that of $D20_{[EQ]}$. The lagged response of the D20 along 6°N to the peak of the $D20_{[EQ]}$ in November is also visible.

The correlations of $D20_{[EQ]}$ with $D20_{[92,6]}$ at 1-month lag and with $D20_{[86,6]}$ at 2-month lag are all 0.96. The strong correlation indicates that equatorial forcing is dominant for the D20 seasonal variability in the Bay through the propagation of the equatorial Kelvin waves and the reflection of Rossby waves. However, as the thermocline variability in the equatorial ocean includes the contribution from both Kelvin waves and Rossby waves, how much does the $D20_{[EQ]}$ in Fig. 7a represent the Kelvin wave signals? The present examination shows that the signal in $D20_{[EQ]}$ consists predominantly of Kelvin wave signal because $D20_{[EQ]}$ and $USTR_{[EQ]}$ are in phase and the amplitude of the D20 anomalies is rather proportional to the amplitude of the zonal wind stress. (Fig. 7b). The zero lag correlation between $D20_{[EQ]}$ and $USTR_{[EQ]}$ at 0.90 indicates that the contribution from Rossby waves generated either by local forcing or by reflection from the eastern boundary is minimal. The local Rossby waves, if they were significant, would cancel out the anomalies induced by Kelvin waves, because the D20 anomalies associated with Rossby waves have a sign opposite to the anomalies associated with Kelvin waves (i.e., westerly (easterly) winds generate downwelling (upwelling) Kelvin waves and upwelling (downwelling) Rossby waves). The reflected Rossby waves, if they were significant, would cause the response of the D20 anomalies lagging the local wind-stress anomalies.

3.5. The "biased" SSH signals due to salinity effects

We had hoped that T/P SSH observations would be a useful data source for tracking propagating wave signals because of their basin-wide coverage and intimate connection to the thermocline variability. However, the plot of the SSHs (Fig. 8) at the three equatorial and interior Bay locations used to construct the $D20_{[EQ]}$, $D20_{[86,6]}$ and $D20_{[92,6]}$ shows that the SSH variability is not identical to the D20 variability.

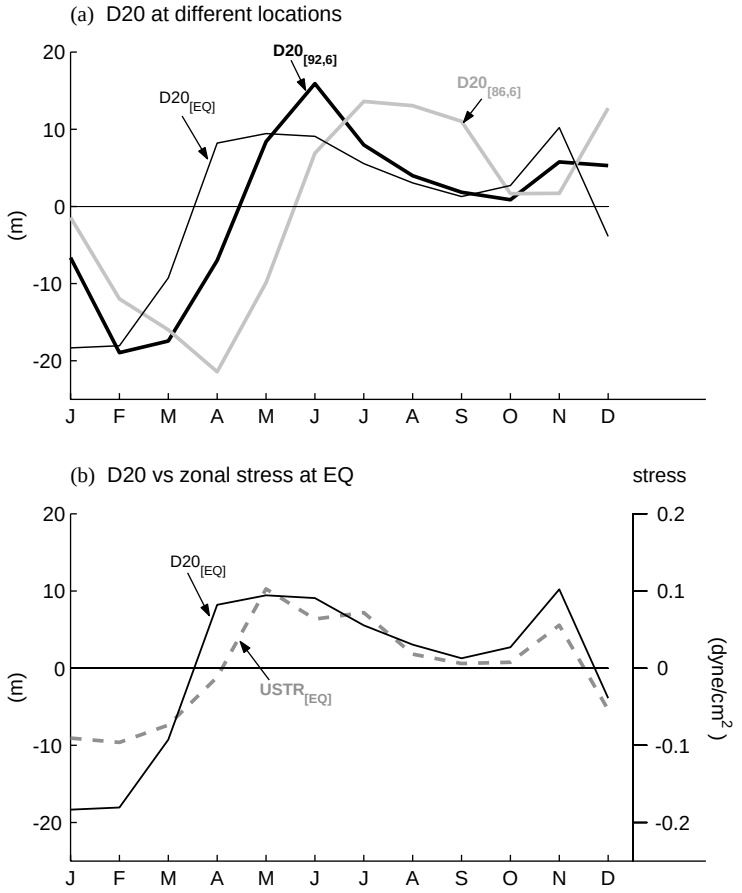

Fig. 7. Annual cycle of (a) seasonal D20 variations at different locations and (b) seasonal D20 and zonal wind-stress variations at the chosen equatorial position. The variables represent seasonal anomalies from the annual mean.

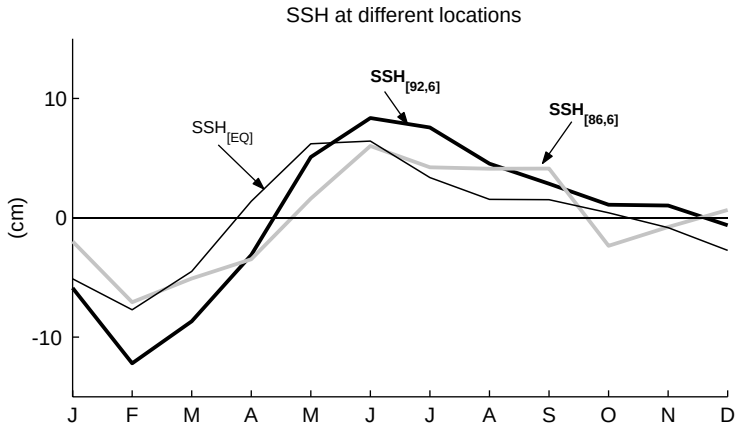

Fig. 8. Annual cycle of seasonal SSH variations (annual mean removed) at different locations.

Compared to the D20s (Fig. 7a), the semiannual periodicity is less obvious in the SSHs because the peak in the fall does not stand out, and the phase lag relationship between the variability at the equator and at 6°N does not hold from July to December. Further comparison of the evolution of the SSH (Fig. 9a) and D20 (Fig. 6a) along 6°N indicates that the temporal variability of the two are similar, with low (negative) SSH corresponding to shallow (negative) D20 and vice versa, but the characteristics of the variability have two major differences. First, the SSH anomalies are broad and more zonally aligned, quite unlike the D20 anomalies that are narrowly confined with prominent westward propagation. Second, the SSH has predominantly positive anomalies from May to November for the eastern half of the section. The negative (upwelling) phase of the D20 that leaves the eastern boundary in August is hardly identifiable in the SSH plot. The differences warrant a reexamination of the relationship between SSH and the D20.

SSH represents the change of buoyancy in the water column due to changes of temperature and salinity. Because of the assumption that the temperature effects associated with the change of the thermocline are several times larger than the salinity effects associated with the change of the halocline, the SSH variability is usually taken as the thermocline variability. However, the Bay is the freshest region in the Indian Ocean. The peninsular river runoffs combined with direct precipitation during the southwest monsoon bring about 0.1 Sv of fresh water to the Bay on an annual basis (Murty et al, 1992; Varkey et al., 1996). The large amount of freshwater input has major impact on near-surface water properties, stratification, and circulation (Sprintall and Tomczak, 1992; Conkright et al., 1999; Han et al., 2001; Howden and Murtugudde, 2001). Evidence is found in the western tropical Pacific, where salinity imposes significant influence on the vertical distribution of heat (Lukas and Lindstrom, 1991), that the linear relationship between SSH and thermocline variability does not hold (Ji et al., 2000). It is highly likely that the lack of the representation of the thermocline variability by

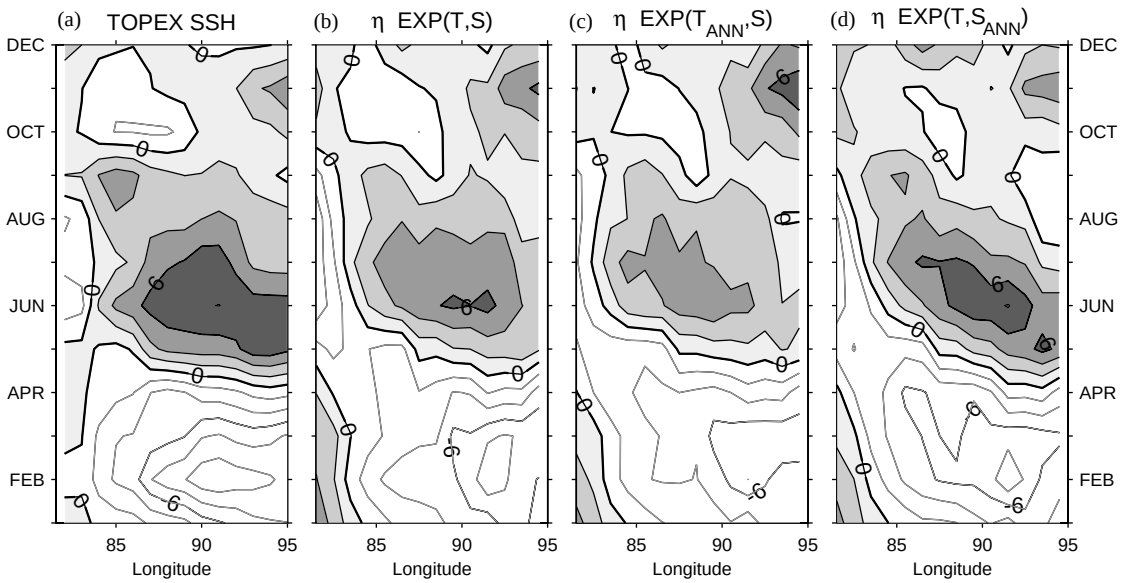

Fig. 9. Seasonal variations (annual mean removed) of SSH (a) observed from satellite altimeter, (b) derived from EXP(T, S) that includes the effects of seasonal temperature and salinity on density, (c) derived from EXP(T_{ANN}, S) that includes only the effects of seasonal salinity on density, and (d) derived from EXP(T, S_{ANN}) that includes only the effects of seasonal temperature on density. The contour interval is 2 cm for all plots. Positive anomalies are shaded and negative anomalies are contoured with gray lines.

SSH observations along 6°N in the Bay is caused by the large salinity fluctuation associated with monsoon rainfall.

Here we attempt to use the $1\frac{1}{2}$-layer model configuration (Fig. 2d) to explore the relationship between SSH and thermocline variability under salinity influence. As is known, the layer densities ρ_1 and ρ_2 are conventionally assumed to be constant in most applications of the $1\frac{1}{2}$-layer model (e.g., Luther and O'Brien, 1985; Yu et al., 1991). To take into account the effects of seasonal salinity as well as those of seasonal temperature on the near-surface density, we let the upper-layer density ρ_1 to be a function of time and location, while keeping the lower-layer density ρ_2 a constant. In this case, ρ_1 can be written in the following form:

$$\rho_1(x,t) = \overline{\rho_1}(x) + \rho_1'(x,t), \tag{4}$$

where the bar denotes the temporal mean and prime denotes the departure from the mean. As the D20 is a good proxy for the pycnocline variability (Figs. 2a–c), ρ_1 is calculated by using the temperature and salinity averaged from the surface to the D20. The temperature is taken from the compiled XBTs, while the salinity is from the WOA monthly climatology. Using the concept of the $1\frac{1}{2}$-layer model, the relationship between the sea-level variability, $\eta'(x,t)$, and the variability of the D20 at the interface between the two layers, $h_d'(x,t)$, is obtained as

$$\eta'(x,t) \approx -\frac{\rho_1'(x,t)}{\rho_1(x)} H(x) + \frac{\rho_2 - \overline{\rho_1}(x)}{\rho_2} h_d'(x,t), \tag{5}$$

where $H(x)$ is used as the annual mean of the D20. The first term on the right-hand-side of (5) represents the contribution from the density perturbation and the second term quantifies the effect of the interfacial displacement on the sea-level variability. If ρ_1 is constant (i.e., $\rho_1' = 0$), then $\eta'(x,t)$ is determined by the second term, which is $\eta'(x,t) \approx [(\rho_2 - \overline{\rho_1}(x))/\rho_2] h_d'(x,t)$. This returns the commonly used relationship between the sea-surface level and thermocline variability in the layer models.

By using (5), the seasonal variations of sea level are computed at 6°N with three temperature–salinity ($T-S$) combinations: monthly T and monthly S (referred to as Exp(T,S)), annual T and monthly S (referred to as Exp(T_{ANN},S)), and monthly T and annual S (referred to as Exp(T,S_{ANN})). Results from the three experiments were plotted in Figs. 9b–d along with the T/P SSH observations (Fig. 9a). Amazingly, Exp(T,S) (Fig. 9b) that includes the seasonal effects of both temperature and salinity yields an SSH structure very similar to the one from the satellite altimeter (Fig. 9a): the broad zonal alignment is well produced and the upwelling phase in the fall is absent in the eastern half of the section! As is seen from Exp(T_{ANN},S) and Exp(T,S_{ANN}), these features are caused by salinity effects. The exclusion of temperature variations in Exp(T_{ANN},S) (Fig. 9c) weakens only the amplitude of the sea-level anomalies but gives no major structural difference compared to Exp(T,S) (Fig. 9b). However, the picture is quite different when excluding the salinity variations in Exp(T,S_{ANN}) (Fig. 9d). The estimated sea level, in which the westward propagation and semiannual periodicity of the D20 characteristics are clearly represented, resembles closely the D20 (Fig. 6a) not the T/P SSH (Fig. 9a).

There is no doubt that salinity has considerable impact on the SSH variability at 6°N in the Bay. The suppression of the upwelling signal in the fall might well be due to the large input of fresh water, as the low salinity increases the buoyancy of the water column and elevates the SSH, compensating the upwelling effect imposed by the remote forcing signal. By using (5), it is estimated that the contribution of the seasonal salinity fluctuation to SSH variations is up to 3 cm based on the WOA salinity climatology, which equals the contribution of the seasonal temperatures.

4. Interannual variability

4.1. Characteristics of variability

The time–longitude plot of the D20 (annual mean removed) along 6°N during 1988–1999 is shown in Fig. 10a. Low-frequency variability is evident, albeit some noise is present. The most striking feature is that the D20 variability was dominated by a clear semiannual cycle in late

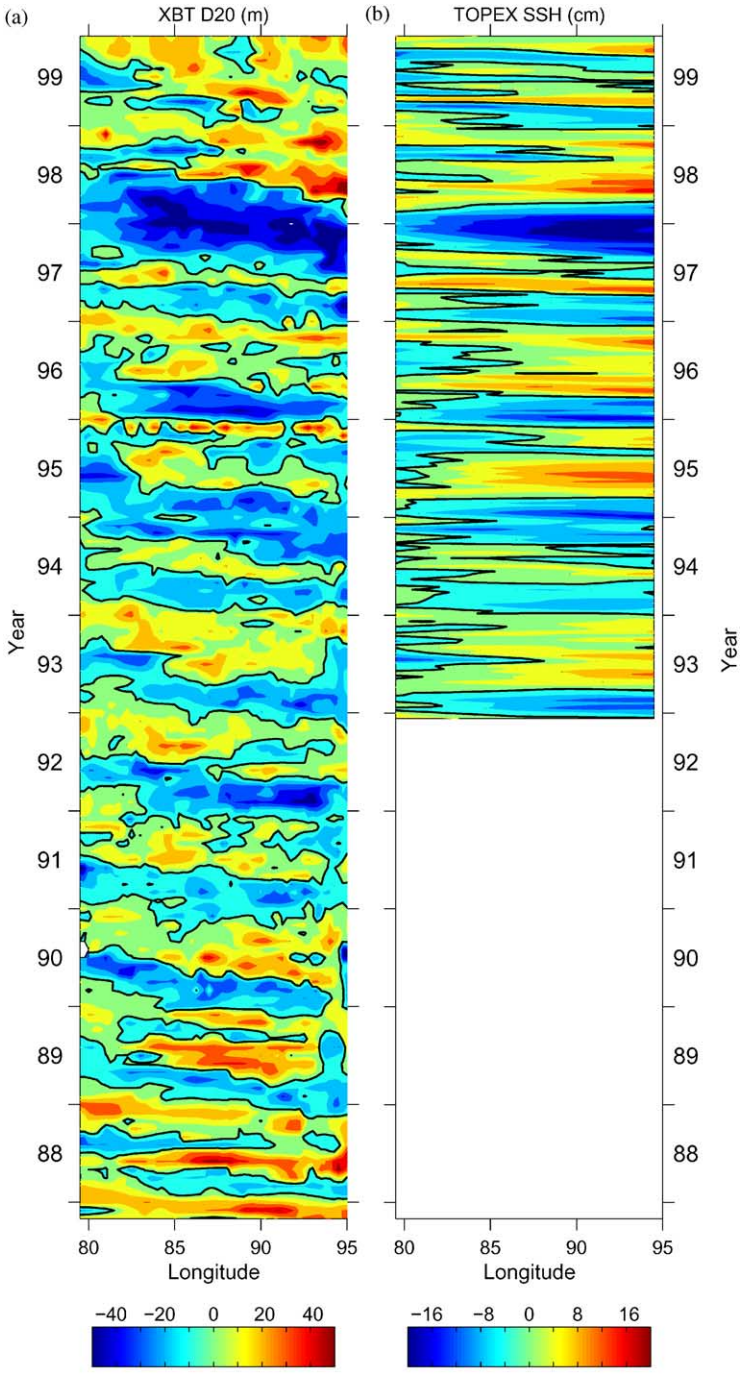

Fig. 10. (a) Variations of D20 (annual mean removed but seasonal cycle retained) from the XBT observations for the period 1988–1999 (ci = 10 m) and (b) variations of SSH (only the mean relative to the mean state of 1993 is removed) for the period of 1993–1999 (ci = 4 cm). The zero line is highlighted.

1980s, while it was characterized more by annual cycle in most years of 1990s, with one upwelling phase (negative anomalies) in the first half of the year and a broad downwelling phase (positive anomalies) in the second half of the year. The semiannual cycle appeared to resume after 1997 but the record is too short to be certain. It appears that the shift of the frequency regime in the 1990s was caused by the weakening of the upwelling phase in the fall in some years (such as 1990 and 1992) and by the lack of the downwelling phase in the winter in some other years (such as 1991, 1994 and 1997). The change was most dramatic in 1994 and 1997, when an unusually intense upwelling event developed in the summer that not only completely shut down the downwelling phase in the following winter but also continued to strengthen the upwelling phase of the next spring.

The time–longitude plot of the SSH anomalies (the mean relative to 1993–1996 removed) at 6°N for the period of 1993–1999 was shown (Fig. 10b). The interannual variability of SSH is quite similar to that of the D20 with both showing profound upwelling anomalies in 1994 and 1997. The effect of salinity on the zonal alignment of the SSH anomalies is apparent. Apart from this, the salinity signature in the SSH structure on interannual timescales is not known because of the lack of salinity observations. But the similarity between the signs of the SSH and D20 anomalies suggests that the SSHs represent reasonably well the tendency of interannual thermocline variations.

4.2. Relation to remote and local wind variability

On interannual timescales, the Indian Ocean has a fairly distinct tropospheric biennial oscillation (TBO) (Meehl, 1987), a complex relationship to El Niño southern oscillation (ENSO) (Barnett, 1983; Shukla, 1987; Webster and Yang, 1992; Halpern and Woiceshyn, 2001), and the Indian dipole mode event in the equatorial region (Saji et al., 1999; Webster et al., 1999; Yu and Rienecker, 1999, 2000). The 1990s were marked by a decade of profound climate anomalies, among which the series of ENSO events in the Pacific Ocean and strong dipole mode events of 1994 and 1997 in the Indian Ocean are most notable. These events triggered coupled atmosphere–ocean interactions in the equatorial Indian Ocean and generated easterly wind anomalies. It has been documented that the development of the anomalies started in the summer associated with the seasonal migration of the southeast trade winds toward the equator and matured in the fall.

It appears that the weakening/disappearing of the downwelling phase in the winter during the 1990s was directly related to the change of the equatorial zonal winds. To examine this relationship, the time series of the $D20_{[92,6]}$ and $USTR_{[EQ]}$ for the period 1988–1999 were plotted (Fig. 11a). The TBO signals were clearly displayed with the strength of the zonal wind stress oscillating alternatively between years. Disruption of the TBO signals was seen in the 1990s with prolonged easterly (negative) wind anomalies in 1994 and 1997 and westerly (positive) wind anomalies in 1996 and 1998. The change in the equatorial zonal forcing induced a lagged response in the $D20_{[92,6]}$. The two time series have a maximum correlation at 0.77, with the $D20_{[92,6]}$ lagging the $USTR_{[EQ]}$ by 1 month. Clearly, the 1-month lagged relationship, which governs the connection between the $D20_{[92,6]}$ and $USTR_{[EQ]}$ on seasonal timescales (Fig. 7a), governs also their connection on interannual timescales. This suggests that the equatorial Kelvin waves are an effective mechanism of transmitting the equatorial wind variability into the Bay on both seasonal and interannual timescales.

The local Ekman pumping W_E (Fig. 11b) appears to be a secondary contributor to the $D20_{[92,6]}$ variability. The correlation is 0.25 with zero lag and is maximum, 0.56, with W_E leading the $D20_{[92,6]}$ by 4 months. Theoretically, the curl anomalies have a $\frac{1}{4}$ phase (6 months for an interannual signal) relationship with the $D20_{[92,6]}$ anomalies because of the bounded dynamical relationship (1). However, the noisy XBT data and other undetermined processes in (1) could alias the phase relationship. Nevertheless, the response of the D20 to Ekman pumping is a lagged response. Figs. 11a and b show that W_E may make a greater contribution to the upwelling anomalies in the $D20_{[92,6]}$ than the remote equatorial forcing in 1992, while it may not dominate

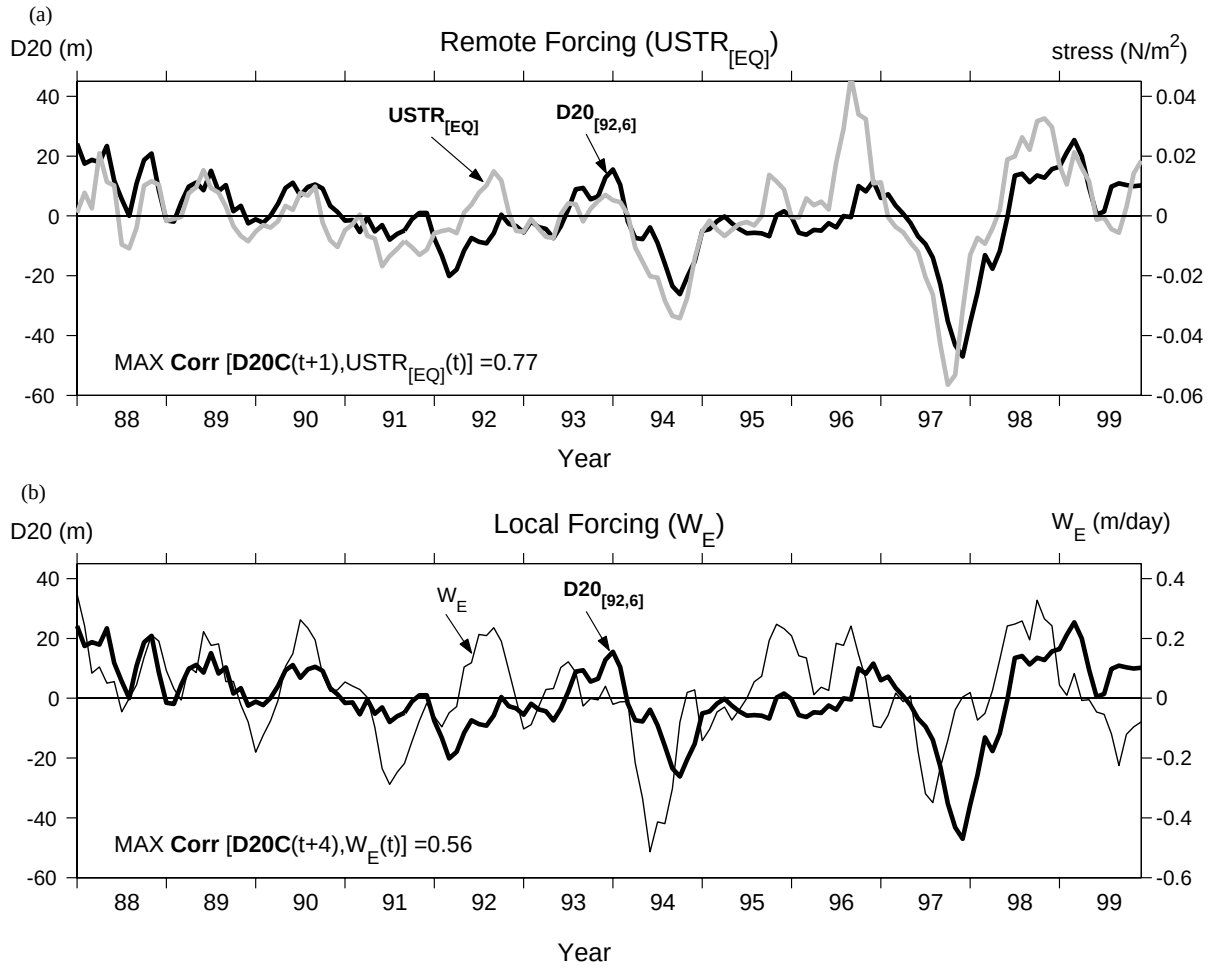

Fig. 11. (a) Time series of $D20_{[92,6]}$ and $USTR_{[EQ]}$ for the period 1988–1999. The maximum correlation is 0.77 when $USTR_{[EQ]}$ leads $D20_{[92,6]}$ by 1 month. (b) Time series of $D20_{[92,6]}$ and local W_E for the period 1988–1999. The maximum correlation is 0.56 when W_E leads $D20_{[92,6]}$ by 4 months. Annual mean is removed from all variables.

remote forcing in 1994 and 1997. The amplitude of the $D20_{[92,6]}$ in the latter 2 years was proportional to the amplitude of the wind forcing $USTR_{[EQ]}$, suggesting that the Indian dipole mode events have a significant effect on the thermocline circulation in the Bay.

4.3. The Bay in 1994 and 1997

The effects of the dipole mode events were felt not merely along 6°N (Figs. 10a and b) but over the entire Bay through the mechanisms of wave propagation and radiation (Figs. 12a and b). The similarity of the dipole mode in its development in 1994 and 1997 has been documented (Saji et al., 1999; Webster et al., 1999). The SSH observations in Figs. 12a and b also indicate a similar pattern of variations in the Bay in these 2 years. At the height of the event in the fall (a cycle in November is shown), the association of equatorial SSH anomalies with the wave structure is evident: the positive anomalies with downwelling Rossby waves in the west and negative anomalies with upwelling Kelvin waves in the east. In the Bay, poleward propaga-

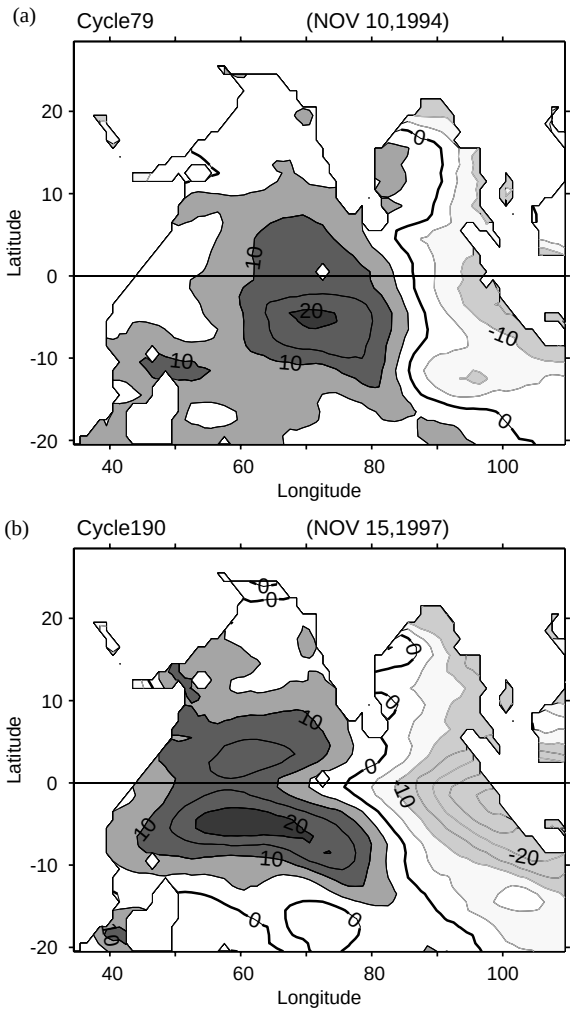

Fig. 12. The influence of the equatorial forcing on the upper-ocean circulation in the Bay seen from SSH observations during the dipole mode events in (a) November 1994 and (b) November 1997. The contour interval is 5 cm. Anomalies are darkly shaded if >5 cm and lightly shaded if <5 cm.

tion of upwelling coastal Kelvin waves is identifiable by the presence of large negative SSH anomalies along the periphery of the Bay, and the radiation of upwelling Rossby waves is seen by the southwestward extension of the negative anomalies. Clearly, the strong dipole mode events in 1994 and 1997 (Vinayachandran et al., 1999b; Reppin et al., 1999; Murtugudde et al., 2000) resulted in a strong upwelling event in the Bay.

5. Summary and discussion

The D20 observed from XBTs along 6°N in the Bay showed pronounced seasonal-to-interannual variability and profound westward propagation. But not all the D20 characteristics are depicted by satellite SSH observations. The cause of the thermocline variability for the period of 1988–1999 and the relationship to SSH variability were analyzed in this study with the addition of the SSMI wind product and WOA salinity analysis. Two issues were emphasized, i.e. the combined pattern of local and remote forcing in causing the thermocline variability on seasonal-to-interannual timescales and the quantification of the effect of salinity variations on SSH. A two-layer system was introduced to allow equations that govern the essential physics of the thermocline variations to be determined and the relationship between thermocline and sea level to be formulated.

On seasonal timescales, the role of remote forcing and its combination with local forcing were investigated using a vorticity equation that describes low-frequency, basin-scale, β-plane dynamics for a two-layered ocean. This analysis obtained a pattern of interaction between local and remote forcing signals. It was found that the phase of the D20 variability is determined by the phase of the remote signal propagating from the eastern boundary but the amplitude is determined by the interaction with the local Ekman pumping effect. The local forcing enhances the westward propagation of the remote signal that leaves the eastern boundary during the first half of the year but suppresses the remote signal that leaves during the second half of the year, resulting in the differences in the amplitude of the two cycles in the D20. This analysis indicated that the calculation of the Ekman pumping velocity should include the contribution from not only wind-stress curl but also zonal wind stress due to β-effect at 6°N. Omitting the latter would augment the effect of local forcing. This analysis also yielded a lagged phase correlation between the D20 at 6°N and the D20 averaged at the eastern equatorial location within [86–87°E, 1°S–1°N] and a zero-lag correlation between the D20 and the zonal equatorial wind stress at the latter location. These phase

relationships further substantiate the role of the remote equatorial forcing in the thermocline variations along 6°N in the Bay through the eastward propagation of wind-excited Kelvin waves along the equator and the radiation of Rossby waves from poleward propagating coastal Kelvin waves that are formed by the reflection of equatorial Kelvin waves at the eastern boundary.

On interannual timescales, the present analysis found that the D20 at 6°N is most sensitive to the remote interannual wind variability along the equator. For the 12-year XBT record in this study, the D20 was affected greatly by the two Indian Ocean dipole mode events in 1994 and 1997. The prolonged equatorial easterly wind anomalies shut down completely the downwelling phase of the D20 in late fall, leading to profound upwelling over the entire section. The lag correlation between the D20 at 6°N and the equatorial zonal wind stress is very high (>0.77) over the 12-year period. The local wind forcing appears to be a secondary contributor to the interannual variability of the D20.

The relationship between satellite SSH and the D20 is not linear at 6°N in the Bay. Two major structural differences have been identified. First, the SSH anomalies are more zonally aligned and less westward propagating. Second, the cycle in the first half of the year is much broadened, while the cycle in the second half of the year, particularly the upwelling phase, is reduced considerably, leading to a weak semiannual signal in SSH. By allowing the density in the upper layer of the two-layered model to include the seasonal changes of temperature and salinity, the study has successfully produced the SSH structure from XBT temperature and WOA salinity data. Sensitivity tests clearly indicated that the zonal alignment and weak semiannual signal are the result of the salinity. Using the WOA salinity, it is estimated that at 6°N the maximum amplitude of the SSH variations induced by the salinity effect is about 3 cm, equivalent to the amplitude induced by the temperature effect.

The study showed clearly the important role of remote equatorial forcing in the D20 variability at 6°N in the Bay on both seasonal and interannual timescales. It also showed the nonnegligible effect of the salinity variations on the SSH observations. So caution should be exercised in interpreting the thermocline variability and in determining wave properties in the Bay from SSH observations.

Acknowledgements

Support for this study by the WHOI Independent Study Award is acknowledged. The XBT profiles from 1990 onward were taken from the database of the Global Temperature–Salinity Profile Program and those before 1990 from the archive of the Global Temperature and Salinity Subsurface Data Centre (Brest, France). I thank Chet Koblinsky for providing the gridded SSH observations via anonymous ftp to iliad.gsfc.nasa.gov and Bob Atlas and Joe Ardizzone for the SSMI wind analysis via anonymous ftp to podaac.jpl.nasa.gov. This is contribution 10577 from the Woods Hole Oceanographic Institution.

References

Atlas, R., Hoffman, R., Bloom, S., Jusem, J., Ardizzone, J., 1996. A multi-year global surface wind velocity data set using SSM/I wind observations. Bulletin of the American Meteorological Society 77 (5), 869–882.

Barnett, T.P., 1983. Interaction of the monsoon and pacific trade wind system at interannual time scales. Part I: the equatorial zone. Monthly Weather Review 111, 756–773.

Basu, S.K., Meyers, S.D., O'Brien, J.J., 2000. Annual and interannual sea level variations in the Indian Ocean from TOPEX/POSEIDON observations and ocean model simulations. Journal of Geophysical Research 105, 975–994.

Cane, M.A., Sarachik, E., 1981. The response of a linear baroclinic ocean to periodic forcing. Journal of Marine Research 39, 651–693.

Clarke, A.J., Liu, X., 1993. Observations and dynamics of semiannual and annual sea levels near the eastern equatorial Indian Ocean boundary. Journal of Physical Oceanography 23, 386–399.

Conkright, M.E., Levitus, S., O'Brien, T., Boyer, T.P., Stephens, C., Johnson, D., Baranova, O., Antonov, J., Gelfeld, R., Rochester, J., Forgy, C., 1999. World Ocean Database 1998: Documentation and Quality Control, Version 2.0. Ocean Climate Laboratory National Oceanographic Data Center, Silver Spring, MD. National Oceanographic Data Center Internal Report 14.

Eigenheer, A., Quadfasel, D., 2000. Seasonal variability of the Bay of Bengal circulation inferred from TOPEX/POSEIDON altimetry. Journal of Geophysical Research 105, 3243–3252.

Fu, L.L., Cheney, R.E., 1995. Application of satellite altimetry to ocean circulation studies: 1987–1994. Reviews of Geophysics, Supplement, US National Report to International Union of Geodesy and Geophysics 1991–1994, pp. 213–223.

Hacker, P., Firing, E., Hummon, J., Gordon, A., Kindle, J.C., 1998. Bay of Bengal currents along the northeast monsoon. Geophysical Research Letters 25, 2769–2772.

Halpern, D., Woiceshyn, P.M., 2001. Somali Jet in the Arabian Sea, El Niño, and India rainfall. Journal of Climate 14, 434–441.

Han, W., McCreary, J.P., Kohler, K.E., 2001. Influence of P-E and Bay of Bengal rivers on dynamics, thermodynamics, and mixed-layer physics in the upper Indian Ocean. Journal of Geophysical Research 106, 6895–6916.

Howden, S.D., Murtugudde, R., 2001. Effects of river inputs into the Bay of Bengal. Journal of Geophysical Research 106, 19825–198843.

Ji, M., Reynolds, R.W., Behringer, D., 2000. Use of Topex/Poseidon sea level data for ocean analyses and ENSO prediction: some early results. Journal of Climate 13, 216–231.

Kessler, W.S., 1990. Observations of long Rossby waves in the northern tropical Pacific. Journal of Geophysical Research 95, 5183–5217.

Koblinsky, C.J., Beckley, B.D., Ray, R.D., Brenner, A.C., Tsaoussi, L.S., Wang, Y.M., Williamson, R.G., 1998. NASA Ocean Altimeter Pathfinder Project, Report 1: Data Processing Handbook. NASA Technical Memorandum-1998-208605.

Koblinsky, C.J., Beckley, B.D., Ray, R.D., Brenner, A.C., Tsaoussi, L.S., Wang, Y.M., 1999. NASA Ocean Altimeter Pathfinder Project, Report 2: Data Set Validation. NASA Technical Memorandum-1999-209230.

Levitus, S., Boyer, T., 1994. World Ocean Atlas 1994, Vol. 3: Salinity. NOAA Atlas NESDIS 3, US Government Printing Office, Washington, DC, 93pp.

Lighthill, M.J., 1969. Dynamics response of the Indian Ocean to the onset of the southwest monsoon. Philosophical Transactions of the Royal Meteorological Society A265, 45–92.

Lukas, R., Lindstrom, E., 1991. The mixed layer of the western equatorial Pacific Ocean. Journal of Geophysical Research 96 (Suppl.), 3343–3357.

Luther, M.E., O'Brien, J.J., 1985. A model of the seasonal circulation in the Arabian Sea forced by observed winds. Progress in Oceanography 14, 353–385.

Maes, C., 1998. Estimating the influence of salinity on sea-level anomaly in the ocean. Geophysical Research Letters 25, 3551–3554.

Masumoto, Y., Meyers, G., 1998. Forced Rossby waves in the southern tropical Indian Ocean. Geophysical Research Letters 103, 27589–27602.

McCreary, J.P., Kundu, P.K., Molinari, R.L., 1993. A numerical investigation of dynamics, thermodynamics and mixed-layer processes in the Indian Ocean. Progress in Oceanography 31, 181–244.

McCreary, J.P., Han, W., Shankar, D., Shetye, S.R., 1996. Dynamics of the East India Coastal Current. 2. N umerical solutions. Journal of Geophysical Research 101, 13993–14010.

Meehl, G.A., 1987. The annual cycle and interannual variability in the tropical Pacific and Indian Ocean regions. Monthly Weather Review 115, 27–50.

Meyers, G., 1975. Seasonal variation in transport of the Pacific north equatorial current relative to the wind field. Journal of Physical Oceanography 5, 442–449.

Meyers, G., 1979. On the annual Rossby wave in the tropical North Pacific Ocean. Journal of Physical Oceanography 9, 663–674.

Millero, F.J., Poisson, A., 1981. International one-atmosphere equation of state of seawater. Deep-Sea Research 28A, 625–629.

Murtugudde, R., McCreary, J.P., Busalacchi, A.J., 2000. Oceanic processes associated with anomalous events in the Indian Ocean with relevance to 1997–1998. Journal of Geophysical Research 105, 3295–3306.

Murty, V.S.N., Sarma, Y.V.B., Rao, D.P., Murty, C.S., 1992. Water characteristics, mixing and circulation in the Bay of Bengal during southwest monsoon. Journal of Marine Research 50, 207–228.

Pedlosky, J., 1996. Ocean Circulation Theory. Springer, Berlin, Heidelberg, 453pp.

Potemra, J.T., Luther, M.E., O'Brien, J.J., 1991. The seasonal circulation of the upper ocean in the Bay of Bengal. Journal of Geophysical Research 96, 12667–12683.

Reppin, J., Schott, F.A., Fischer, J., Quadfasel, D., 1999. Equatorial currents and transports in the upper central Indian Ocean: annual cycle and interannual variability. Journal of Geophysical Research 104, 15495–15514.

Saji, N.H., Goswami, B.N., Vinayachandran, P.N., Yamagata, T., 1999. A dipole in the tropical Indian Ocean. Nature 401, 360–363.

Schott, F.A., McCreary, J.P., 2001. The monsoon circulation of the Indian Ocean. Progress in Oceanography 51, 1–123.

Schott, F.A., Reppin, J., Fisher, J., Quadfasel, D., 1994. Currents and transports of the Monsoon Current south of Sri Lanka. Journal of Geophysical Research 99, 25127–25141.

Shankar, D., McCreary, J.P., Han, W., Shetye, S.R., 1996. Dynamics of the East India Coastal Current. 1. Analytic solutions forced by interior Ekman pumping and local alongshore winds. Journal of Geophysical Research 101, 13975–13991.

Shetye, S.R., Gouveia, A.D., Shenoi, S.S.C., Sundar, D., Michael, G.S., Nampoothiri, G., 1993. The western boundary current of the seasonal subtropical gyre in the Bay of Bengal. Journal of Geophysical Research 98, 945–954.

Shukla, J., 1987. Interannual variability of monsoons. In: Fein, J.S., Stephens, P.L. (Eds.), Monsoons. Wiley, New York, pp. 523–548.

Sprintall, J., Tomczak, M., 1992. Evidence of the barrier layer in the surface layer of the Tropics. Journal of Geophysical Research 97, 7305–7316.

UNESCO, 1981. Tenth Report of the Joint Panel on Oceanographic Tables and Standards. UNESCO Technical Papers in Marine Science, No. 36, p. 24.

Varkey, M.J., Murty, V.S.N., Suryanarayana, A., 1996. Physical oceanography of the Bay of Bengal and Andaman Sea. Oceanography and Marine Biology 34, 1–70.

Vinayachandran, P.N., Yamagata, T., 1998. Monsoon response of the sea around Sri Lanka: generation of thermal domes and anticyclonic vortices. Journal of Physical Oceanography 28, 1946–1960.

Vinayachandran, P.N., Masamoto, Y., Mikawa, T., Yamagata, T., 1999a. Intrusion of the southwest monsoon current into the Bay of Bengal. Journal of Geophysical Research 104, 11077–11085.

Vinayachandran, P.N., Saji, N.H., Yamagata, T., 1999b. Response of the equatorial Indian Ocean to an unusual wind event during 1994. Geophysical Research Letters 26, 1613–1619.

Webster, P.J., Yang, S., 1992. Monsoon and ENSO: selectively interactive systems. Quarterly Journal of the Royal Meteorological Society 1118, 877–926.

Webster, P.J., Moore, A.M., Loschnigg, J.P., Leben, R.R., 1999. Coupled ocean–atmosphere dynamics in the Indian Ocean during 1997–98. Nature 401, 356–359.

White, B.W., 1977. Annual forcing of baroclinic long waves in the tropical North Pacific Ocean. Journal of Physical Oceanography 7, 50–61.

Yang, J., Yu, L., Koblinsky, C.J., Adamec, D., 1998. Dynamics of the seasonal variations in the Indian Ocean from TOPEX/POSEIDON sea surface height and an ocean model. Geophysical Research Letters 25, 1915–1918.

Yu, L., Rienecker, M.M., 1999. Mechanisms for the Indian Ocean warming during the 1997-98 El Niño. Geophysical Research Letters 26, 735–738.

Yu, L., Rienecker, M.M., 2000. Indian Ocean warming of 1997–1998. Journal of Geophysical Research 105, 16923–26939.

Yu, L., O'Brien, J.J., Yang, J., 1991. On the remote forcing of the circulation in the Bay of Bengal. Journal of Geophysical Research 96, 20449–20454.